

Multimodal Hyperspectral Image Classification via Interconnected Fusion

Lu Huo, Jiahao Xia, Leijie Zhang, Haimin Zhang, Min Xu
Faculty of Engineering and IT, University of Technology Sydney

Abstract—Existing multiple modality fusion methods, such as concatenation, summation, and encoder-decoder-based fusion, have recently been employed to combine modality characteristics of Hyperspectral Image (HSI) and Light Detection And Ranging (LiDAR). However, these methods consider the relationship of HSI-LiDAR signals from limited perspectives. More specifically, they overlook the contextual information across modalities of HSI and LiDAR and the intra-modality characteristics of LiDAR. In this paper, we provide a new insight into feature fusion to explore the relationships across HSI and LiDAR modalities comprehensively. An Interconnected Fusion (IF) framework is proposed. Firstly, the center patch of the HSI input is extracted and replicated to the size of the HSI input. Then, nine different perspectives in the fusion matrix are generated by calculating self-attention and cross-attention among the replicated center patch, HSI input, and corresponding LiDAR input. In this way, the intra- and inter-modality characteristics can be fully exploited, and contextual information is considered in both intra-modality and inter-modality manner. These nine interrelated elements in the fusion matrix can complement each other and eliminate biases, which can generate a multi-modality representation for classification accurately. Extensive experiments have been conducted on three widely used datasets: Trento, MUUFL, and Houston. The IF framework achieves state-of-the-art results on these datasets compared to existing approaches.

Index Terms—Hyperspectral Image Classification, Light Detection And Ranging, multi-modal, multi-modalities, multi-sensor information fusion, feature fusion, remote sensing, transformer.

I. INTRODUCTION

Hyperspectral image (HSI) contains enormous spectral information in each pixel [1], [2], which enables the extraction of fine features to identify the material on the earth's surface [3], [4], [5]. However, lacking altitude information, HSI has hardly been used to identify objects with occlusions, such as clouds. Using HSI data to differentiate the same object from similar categories, such as grass on the roof or grass on the ground, is impossible due to different altitudes [6], [7]. Capturing altitude information, Synthetic Aperture Radar (SAR) [8], [9] or Light Detection And Ranging (LiDAR) [10] collaborating with HSI signal are used to detect objects with occlusions or even totally hidden behind obstacles. Thus, the integration of different modalities has attracted increasing research attention in the field of remote sensing.

Most multi-modality fusion methods encode feature representations for one modality and then fuse the features of multiple modalities for classification [11], [12], [13]. Traditional feature fusion approaches, such as concatenation, summation,

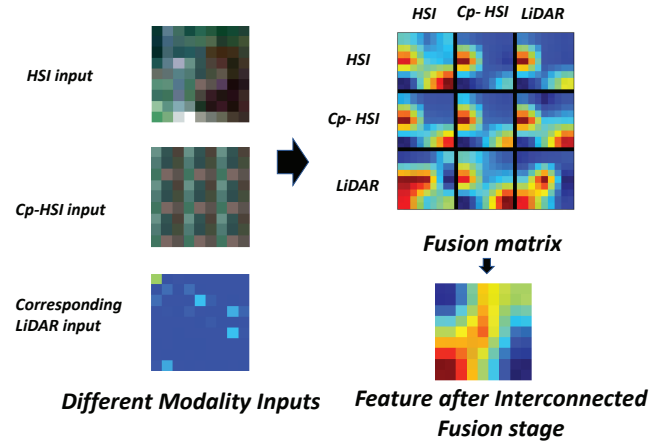


Fig. 1. The grass sample consists of three inputs, including the HSI, the center patch of the HSI (cp-HSI), and the corresponding LiDAR signals. The green part in false color images of the HSI signal presents the grass part while the brown color shows the soil area. These three inputs can generate nine interconnected perspectives for HSI-LiDAR signals. Moreover, these nine interrelated views can complement each other and work together to generate the integrated feature, which can eliminate the bias from each perspective and focus on the grass area.

and encoder-decoder-based fusion, consider feature fusion from limited viewpoints, which cannot consider the inter-modality relationship comprehensively [11], [12], [13], [14], [15]. After feature concatenation, the fused neurons from the corresponding intra-modality feature are triggered while neurons from another intra-modality feature are inhibited [6]. Most HSI-LiDAR fusion methods only consider the spatial correlation within a single modality, such as an HSI signal, while neglecting the contextual information among image patches from inter-modality, limiting the final performance. Besides, some of these fusion methods concentrate on the intra-modality relationship within HSI and overlook that in LiDAR, which leads to information deficiency [16]. In addition, existing feature fusion approaches lack generalization ability for unseen training samples and are prone to overfitting [17].

In this paper, we propose an Interconnected Fusion (IF) framework to enrich intra-modality and inter-modality information and obtain a satisfactory data representation, as shown in Fig. 1. We divide HSI input into 3×3 patches, extract the center patch of HSI input, and replicate it to the size of the HSI input as an extra input to our framework. Then, a fusion matrix is introduced to capture and represent the interconnected correlations among three multi-modality

inputs, including HSI, the replicated center patch of HSI, and the corresponding LiDAR through applying self-attention and cross-attention operations. Later, nine interrelated elements in the fusion matrix can work together to accurately generate an integrated feature representation through the feature fusion layer.

Overall, our main contributions are summarised as follows:

- 1) Extracting the center patch of HSI as an extra input to our framework, the contextual information between the center patch and nearby patches can be extracted to enrich the information from intra- and inter-modality.
- 2) Different from traditional fusion methods such as concatenation, summation, and encoder-decoder-based fusion, the nine interconnected elements in the fusion matrix are first introduced as a feature map for HSI-LiDAR signals, which can complement each other and work together to eliminate the bias from each element.
- 3) Compared to other methods, the proposed method outperforms existing methods on three widely used datasets, including Trento, MUUFL, and Houston. In addition, we extend our experiment to study the effects of the change in patch size and fusion strategies, including early, middle, and late. We found that the IF framework can achieve robust performance on different fusion strategies when the input patch has more pixels, which means IF is a robust framework that achieves similar performance in different fusion strategies.

II. RELATED WORK

A. Approaches of single modality signal representation

The commonly used single modality signal representation approaches in the field of HSI are Convolutional Neural Networks (CNN) based methods [18], [11], [19], [12], [20], [13]. Deep CNN with pixel-pair features (CNN-PPF) [18] and 1D-CNN [21] with ℓ_2 regularization employ pixel-pair CNN structure. However, pixel-wise information for the HSI area only explores the spectral feature at the pixel level without any spatial relationship. The spectral data of nearby pixels have similar attributes which is suitable to explore more discrimination power for HSI data [22], [23], [24], [25], [26], [27], [28], [19], [29]. However, suppose the CNN model extracts spectral and spatial information together. In that case, they will pay considerable attention to spatial direction knowledge rather than spectral information, which means a significant amount of hyperspectral information on each pixel is not fully leveraged [30]. Moreover, the CNN-based models have many limitations, such as neglecting long-range dependencies and overlooking the positional information [31].

The Vision Transformer (ViT) [32] achieves better performance than the CNN structure. Moreover, transformer-based models provide more robustness and generalizable features than CNN-based models with fewer parameters and a lower risk of overfitting [33], [34]. SpectralFormer [30] can learn group-wise spectral embeddings from neighboring bands of HSI. Furthermore, some transformer-based methods employ the spectral-spatial transformer architecture to get spatial and

spectral attention together [35], [36]. Unfortunately, the parameters of most transformer-based models are enormous and computationally costly [37]. In addition, the performance of these models relies heavily on large-scale training data [32]. Thus, many challenges remain in training transformer-based models. In our framework, we employ ViT as the backbone to capture general dense visual features [31] coupled with the neighborhood relationship of the center patch and nearby patches to extract the context-related feature. To alleviate the data-hungry limitation of ViT, the depth of our framework is three.

B. Approaches of multiple modality fusion

The feature fusion algorithms in multi-modal HSI fields usually employ traditional fusion methods, including summation, concatenation, encoder-decoder, and cross-fusion [11], [12], [13], [14], [15]. Two-branch CNN employs the two sub-network to extract the features from HSI and LiDAR data respectively and then combine these two different features using concatenation [11]. In addition, the weight sharing for two branch CNNs (Co-CNN) has been applied for HSI and LiDAR feature extraction. After that, these two types of features are fused at the feature level using summation or maximization strategy [20]. Encoder-decoder architecture (EndNet) has been employed in this field. They use an autoencoder to integrate and reconstruct the different modalities' information [12]. Another autoencoder-based model is the Interleaving Perception Convolutional Neural Network (IP-CNN), which employs a bidirectional autoencoder for information fusion, feature extraction, and reconstruction for HSI and LiDAR data sources [13]. Moreover, a shared and specific feature learning (S2FL) model divides the multi-modal HSI data into two broad types, including shared space for different modalities and specific space for each modality [38]. Furthermore, the MDLRS framework employs a compactness-based cross-fusion to get a more diversified relationship from different modalities [6]. However, the feature extracted by CNN structure has a substantial prejudice towards texture and a troubling shortage of positional information [31]. Thereby, the CNN structure remains limited to capturing the global interaction of each element of the input.

Recently, ViT has been applied in HSI multi-model field because ViT can achieve competitive performance compared to CNN. The multimodal fusion transformer (MFT) network combines the characteristics of different modalities through cls token from another modality [39]. Nevertheless, these fusion methods overlook the contextual information for multi-modal signals and the information of the modality itself, which will retain limited performance while our framework extracts intra- and inter-modality with the contextual information between the center patch and the nearby patches.

III. INTERCONNECTED FUSION FRAMEWORK

The proposed IF framework contains three stages: intra-modality feature encoding, interconnected fusion, and classification (see Fig. 2 and Algorithm 1). The first stage employs ViT encoders to extract three intra-modality features

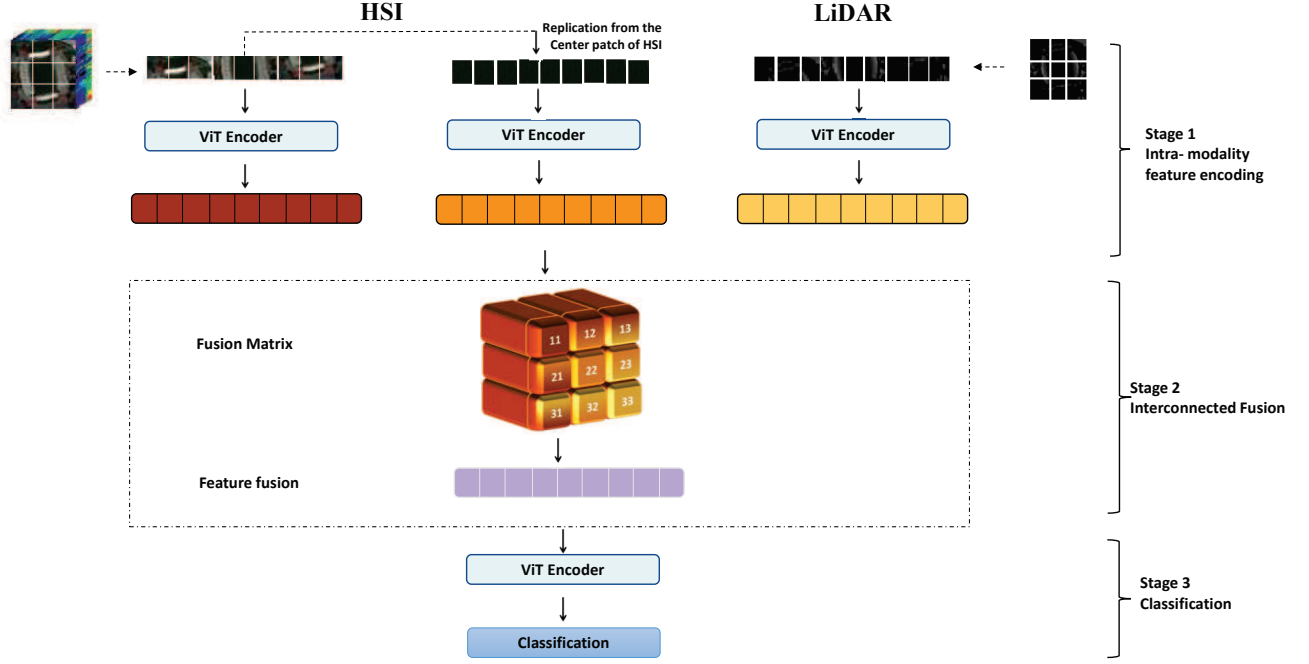


Fig. 2. The proposed IF framework contains three stages: Intra-modality feature encoding, interconnected fusion, and classification. For Intra-modality feature encoding, the center patch of HSI is introduced as an extra input to explore the contextual information between the center patch and nearby patches for intra- and inter-modality. Regarding the interconnected fusion stage, the nine interconnected perspectives in the Fusion Matrix can represent the intra- and inter-modality with contextual information. These nine interrelated views can complement each other and eliminate the bias from each other through the feature fusion layer. For the final stage, the integrated feature can be calculated, and the classification result can be obtained.

for the replicated center patch of HSI input, HSI input, and LiDAR input separately. Then, the second stage introduces the fusion matrix to gather nine perspectives for intra- and inter-modality information through calculating self-attention and cross-attention of three intra-modality features. Afterward, the nine interrelated elements in the Fusion Matrix can complement each other and work as an integrated feature through the feature fusion layer. Moreover, the last stage employs the ViT Encoder to get more abstract integrated features and classification results.

A. Intra-modality feature encoding

For intra-modality feature encoding, the center patch of HSI is introduced as extra input for further exploring the contextual information between the center patch and nearby patches. The inputs contain three data sources, including HSI X_{h1} , the corresponding LiDAR X_l , and the center patch X_{h2} of HSI data feeding to three separate encoders, H , H_p for HSI and the L for LiDAR. The input for HSI and LiDAR has the same patch numbers p and the embedding dimensions D after patch embedding. The data of X_{h2} comes from the center patch of X_{h1} duplicated p times (same patch numbers with HSI and LiDAR sample). Then, the HSI and LiDAR samples are passed through the transformer layer including Multi-head Self-Attention (MSA), Feed-Forward Network (FFN), and Layer Normalization (LN) blocks. The MSA can be calculated by concatenating self-attention (SA) results for different heads

and then projected by a weight matrix W (see Equations 1, 2):

$$MSA(z) = [SA_1(z), \dots, SA_h(z)]W \quad W \in \mathbb{R}^{hD_q \times D} \quad (1)$$

where h is the number of heads for MSA, and $SA(z)$ can be calculated:

$$SA(z) = \text{softmax}\left(\frac{qk^T}{\sqrt{D_q}}\right)v \quad [q, k, v] = zU_{qkv} \quad (2)$$

$$U_{qkv} \in \mathbb{R}^{D \times 3D_q}$$

where q , k , and v mean query, key, and value, respectively. The MSA results \hat{Z}_{h1}^l , \hat{Z}_{h2}^l and \hat{Z}_l^l can be calculated:

$$\hat{Z}_i^l = MSA(LN(Z_i^{l-1})) + Z_i^{l-1} \quad i \in \{h1, h2, l\} \quad (3)$$

Then, the output of MSA can be updated by the FFN block.

$$Z_i^l = MLP(LN(\hat{Z}_i^l)) + \hat{Z}_i^l \quad i \in \{h1, h2, l\} \quad (4)$$

Thus, three different results \hat{Z}_{h1}^l , \hat{Z}_{h2}^l and \hat{Z}_l^l are generated from encoder H , H_p and L , respectively. Furthermore, after Intra-Modality data processing, these three outputs have the same number of patches and dimensional embeddings.

B. Interconnected fusion

The IF framework not only focuses on feature fusion from different modalities but also on leveraging comprehensive

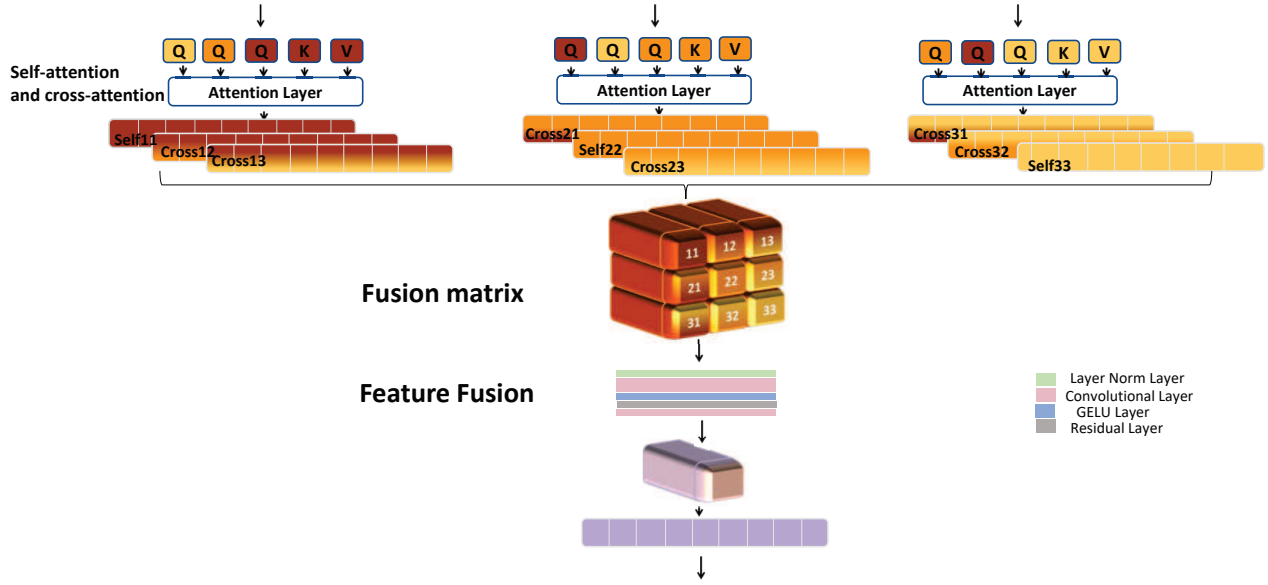


Fig. 3. The interconnected fusion stage utilizes the fusion matrix to gather nine perspectives for intra-modality and inter-modality information with the neighborhood correlation of the center patch and nearby patches. Then, the nine interrelated views in the Fusion Matrix can complement each other and work as an integrated feature through the Feature Fusion layer.

Algorithm 1 The pseudocode for the core of an implementation of IF framework

- 1: **Initialization:** Set $t = 0$, the input data X_{h1} , X_{h2} from HSI data source and X_l from LiDAR data source. Specifically, the center patch of the HSI input X_{h2} is replicated to the same size as the HSI input X_{h1} .
- 2: **for** $t = 0, 1, 2, \dots$, **do**
- 3: **Intra-modality feature encoding:** Extract feature representations Z_{h1}^l , Z_{h2}^l and Z_l^l for the input data X_{h1} , X_{h2} , X_l through ViT encoders separately (refer to Eq.(4);
- 4: **Interconnected Fusion:** calculate **nine interconnected perspectives**:

$$Z_{ij}^c = f_{views}(Z_1^l, Z_2^l, Z_3^l) \quad i, j \in \{1, 2, 3\};$$
 define **fusion matrix**: $Z^m = \begin{bmatrix} Z_{11}^c & Z_{12}^c & Z_{13}^c \\ Z_{21}^c & Z_{22}^c & Z_{23}^c \\ Z_{31}^c & Z_{32}^c & Z_{33}^c \end{bmatrix}$
 calculate **an integrated and corrected feature** \hat{Z}^f and then updated to Z^f (refer to Eq.(9) and Eq.(10);
- 5: **Classification:** Processing the combined feature Z^f through the ViT Encoder (refer to Eqs.(11) and (12)) and getting classification result;
- 6: **end for**

interactions from different modalities. Concerning the interconnected fusion stage, nine interconnected elements in a fusion matrix are proposed to represent the information from intra- and inter-modality and the contextual information across different modalities. The nine interrelated elements in the fusion matrix can complement each other and work as an integrated feature through the feature fusion layer.

First of all, the three intra-modality features Z_{h1}^l , Z_{h2}^l and Z_l^l are calculated in previous stage. Then, nine interconnected perspectives Z_{ij}^c can be generated through self-attention and cross-attention of these three intra-modality features:

$$Z_{ij}^c = f_{views}(Z_{h1}^l, Z_{h2}^l, Z_l^l) \quad i, j \in \{1, 2, 3\} \quad (5)$$

when $i = j$, the self-attention values \hat{Z}_{ij}^c can be calculated by k , q , and v generated from the same input i . On the contrary, when $i \neq j$, cross-attention values \hat{Z}_{ij}^c can be computed by k and v from the same input i while q from another data source j :

$$\hat{Z}_{ij}^c = MSA(q_j, k_i, v_i) + Z_i^l \quad i, j \in \{1, 2, 3\} \quad (6)$$

The value of \hat{Z}_{ij}^c can be updated by residual connection and the FFN block:

$$Z_{ij}^c = MLP(LN(\hat{Z}_{ij}^c)) + \hat{Z}_{ij}^c \quad i, j \in \{1, 2, 3\} \quad (7)$$

Then, the 3×3 fusion matrix can be defined using these nine views.

$$Z^m = \begin{bmatrix} Z_{11}^c & Z_{12}^c & Z_{13}^c \\ Z_{21}^c & Z_{22}^c & Z_{23}^c \\ Z_{31}^c & Z_{32}^c & Z_{33}^c \end{bmatrix} \quad (8)$$

In this fusion matrix, the intra-modality features consist of Z_{11}^c for HSI, Z_{33}^c for corresponding LiDAR, Z_{22}^c for the center patch of HSI, and the HSI relationships between the center patch and nearby patches from two different views Z_{12}^c, Z_{21}^c , separately. Besides, $Z_{13}^c, Z_{31}^c, Z_{23}^c, Z_{32}^c$ show the inter-modality correlations. More specifically, Z_{13}^c and Z_{31}^c represent the relationships of HSI and LiDAR patches at corresponding locations. In contrast, Z_{23}^c and Z_{32}^c provide the correlation across the center patch of the HSI and the nearby LiDAR patches. In addition, $Z_{12}^c, Z_{21}^c, Z_{23}^c, Z_{32}^c$ shows

the contextual information for intra and inter-modality both. Therefore, it is worth noting that nine interconnected elements in the fusion matrix contain the correlations between intra and inter-modality coupled with contextual information.

Each element of the fusion matrix contains bias because of limited information for multi-modal remote sensing signals. The feature fusion layer designed in the IF framework can effectively generate an integrated feature and eliminate the bias from distinct perspectives since these nine interrelated views in the fusion matrix can complement each other (the detailed discussion in Section 4 Ablation study). Then, the 3×3 fusion matrix Z^m can be compacted into an integrated feature \hat{Z}^f :

$$\hat{Z}^f = f_{comp}(Z^m) \quad (9)$$

After that, this feature \hat{Z}^f is updated by the FFN block and residual connection:

$$Z^f = \hat{Z}^f + FFN(\hat{Z}^f) \quad (10)$$

C. Classification

For the classification stage, the integrated result Z^f is treated as a single feature and processed by the ViT encoder:

$$\hat{Z}^u = MSA(LN(Z^f)) + Z^f \quad (11)$$

Moreover, \hat{Z}^u is generated as a result of the MSA block and then processed by the FFN block:

$$Z^u = MLP(LN(\hat{Z}^u)) + \hat{Z}^u \quad (12)$$

Finally, the result Z^u can be calculated. The final classification result can be calculated from the *cls* token.

IV. EXPERIMENTS

This section employs three well-known HSI multi-modal datasets to evaluate the performance of the IF framework. In addition, we compare the performance under different fusion strategies and patches sizes. We study different ablation experiments on the IF framework.

A. Datasets

Houston 2013 Dataset was captured over the University of Houston campus and the nearby urban area in the 2013 IEEE GRSS Data Fusion Contest. This dataset includes HSI and LiDAR-derived Digital Surface Model (DSM) signals. The size of this dataset is 349 by 1905, with a spatial resolution of 2.5m. The HSI signal contains 144 bands from 0.38 to 1.05 μm . Moreover, this dataset consists of fifteen classes, including Grass Healthy, Grass Stressed, Grass Synthetic, Tree, Soil, Water, Residential, Commercial, Road, Highway, Railway, Parking Lot 1, Parking Lot 2, Tennis Court, and Running Track. The training and testing settings for each class are shown in Table I.

Trento Dataset was measured in the rural area of Trento, Italy. The captured size is 600 by 166 pixels, and the spatial resolution is 1m. Furthermore, this dataset contains DSM and HSI signals with six distinct classes: Buildings, Woods, Apple trees, Roads, Vineyard, and Ground. The HSI contains 63

TABLE I
THE STANDARD TRAINING AND TESTING SETS FOR EACH CATEGORY ON HOUSTON DATASET

Class		Number of Samples	
No.	Name	Train	Test
1	Health grass	198	1251
2	Stressed grass	190	1254
3	Synthetic grass	192	697
4	Tress	188	1244
5	Soil	186	1242
6	Water	182	325
7	Residential	196	1268
8	Commercial	191	1244
9	Road	193	1252
10	Highway	191	1227
11	Railway	181	1235
12	Parking lot 1	192	1233
13	Parking lot 2	184	469
14	Tennis court	181	428
15	Running track	187	660
Total		2832	15029

TABLE II
THE STANDARD TRAINING AND TESTING SETS FOR EACH CATEGORY ON TRENTO DATASET.

Class		Number of Samples	
No.	Name	Train	Test
1	Apple trees	129	4034
2	Buildings	125	2903
3	Ground	105	479
4	Woods	154	9123
5	Vineyard	184	10501
6	Roads	122	3174
Total		819	30214

bands from 0.40 to 0.98 μm . The training and testing settings for each class are shown in Table II.

The MUUFL dataset [40] was measured over the University of Southern Mississippi campus in 2010. The size of this dataset is 325 by 220 pixels with 72 bands for the HSI signal. This dataset also contains two different LiDAR signals with different height. In our experiment, we concatenate these two LiDAR signals along the pixel location. Moreover, it contains 11 classes: Trees, Mostly grass, Mixed ground surface, Dirt and Sand, Road, Water, Building Shadow, Building, Sidewalk, Yellow curb, and Cloth panels. The training and testing settings for each class are shown in Table III.

B. Implementation details

We run our model on a Linux system with Intel(R) Xeon(R) Gold 6132 CPU and Nvidia Quadro P5000 GPU. We implement three fusion strategies setting – Early, Middle, and Late on the IF framework. If the number of total layers is N and Stage 1’s layer number is M, the depth of Stage 3 is N-M-1 (see Fig. 4). To alleviate the data-hungry limitation of ViT, the total depth of our framework is three. For the early fusion setting, the depth of Stage 1 is zero, and the layer number of Stage 3 is two. In contrast, for the late fusion setting, the depth of Stage 1 is two, and the layer number of Stage 3 is zero. For the middle fusion setting, the depth of Stage 1 is one, and the layer number of Stage 3 is one. Thus, the setting of fusion strategies for the IF framework can be customized

TABLE III
THE STANDARD TRAINING AND TESTING SETS FOR EACH CATEGORY ON MUUFL DATASET

Class		Number of Samples	
No.	Name	Train	Test
1	Trees	150	23246
2	Mostly grass	150	4270
3	Mixed ground surface	150	6882
4	Dirt and sand	150	1826
5	Road	150	6687
6	Water	150	466
7	Building Shadow	150	2233
8	Building	150	6240
9	Sidewalk	150	1385
10	Yellow curb	150	183
11	Cloth panels	150	269
Total		1650	53687

TABLE IV
THE DETAILED INFORMATION FOR FEATURE FUSION LAYER

Layer No.	Layer type	Detailed setting
1	Layer Norm	Shape [3,3]
2	Convolutional layer	kernel size: (3,3); stride: (1,1); padding: 1
3	Convolutional layer	kernel size: (1,1); stride: (1,1); padding: 0
4	Activate function	GELU()
5	Residual layer	-
6	Convolutional layer	kernel size: (3,3); stride: (1,1); padding: 0

by changing the depth of Stages 1 and 3. Furthermore, we take inspiration from ConvNet [41] to extract the integrated feature effectively. The detailed setting of the feature fusion layer is shown in table IV. Thus, we can get an integrated feature \hat{Z}^f after the feature fusion layer.

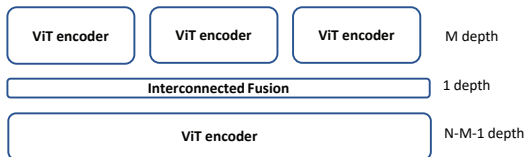


Fig. 4. If the number of total layers is N and Stage 1’s layer number is M, the depth of Stage 3 is N-M-1.

C. Result comparisons

We compare the performance of our method with previous methods – CNN-PPF [18], Two-branch CNN [11], Context CNN [19], EndNet[12], MDL-RS[6], Co-CNN [20], S2FL [38], Spectralformer [30], MFT [39] IP-CNN [13] in Table V, VI, and VII. Within these tables, it is noteworthy that the red values denote the best outcome in the present measurement, whereas the blue values indicate the second-best outcome.

Evaluation on the Houston dataset As shown in Table V, IF achieved the best performance. The overall accuracy (OA), the average accuracy (AA), and the Kappa coefficient of IF are more advantageous than the second-best method (IP-CNN) at around 5%, 3%, and 6%, respectively. Moreover, for most categories, the IF framework can get competitive results,

while IP-CNN achieves the second-best performance, which means IF can gather comprehensive relationships for different modalities without the risk of data leakage like IP-CNN. The implementation of IF results in a notable enhancement of performance by 14%, which suggests that our proposed method is capable of effectively exploring a greater quantity of information in comparison to a single HSI modality. Compared with Two-branch CNN, context CNN, Co-CNN, EndNet, MDL-RS, and S2FL, the result of IF improves 8% since the collection of nine distinct views for HSI-LiDAR signals is found to encompass a wealth of informative details to both intra- and inter-modality relationships, inclusive of contextual information. These nine distinct views serve to address potential biases arising from multiple perspectives. Compared with Spectralformer and MFT, IF markedly improves performance. Even though IF, Spectralformer and MFT both employ the transformer as a backbone, Spectralformer and MFT do not fully explore the characteristics of different modalities, while IF can get comprehensive information for HSI multi-modal data sources.

Evaluation on the MUUFL dataset As shown in Table VI, OA of IF has yielded a favorable result than 4% compared to the second-best IP-CNN. Similarly, the AA and the Kappa of IF perform the best at around 2% and 5% compared with IP-CNN, respectively, which means the IF framework has a remarkable ability to integrate different modalities from diverse perspectives coupled with contextual information. Compared to CNN-PPF, IF improves 7%, which means IF can combine the information of distinct modalities well without influencing the performance of a single HSI modality. Compared with Two-branch CNN, context CNN, Co-CNN, EndNet, MDL-RS, and S2FL, the IF framework gets competitive results because it considers the interaction across distinct modalities from diverse perspectives rather than traditional fusion from limited viewpoints or inadequate interactions of multi-modalities. Compared with Spectralformer and MFT, IF achieves competitive performance since IF contains a wealth of information between distinct modalities.

Evaluation on the Trento dataset As shown in Table VII, the result of IF framework is slightly lower than IP-CNN since IP-CNN needs two-stage training, including unsupervised and supervised training on the same dataset which can cause information leakage. Besides, IF may have an overfitting risk on the fusion matrix to pack plenty of interaction between different modalities. Compared with the other methods, the IF framework can get competitive results showing IF framework has the advantage of exploring comprehensive relationships for distinct modalities and eliminating bias from nine perspectives.

Therefore, the IF framework can achieve the best performance in Trento, MUUFL, and Houston datasets without the risk of data leakage like IP-CNN. Moreover, IF gets competitive results compared to other fusion methods since IF extracts comprehensive characteristics from distinct modalities through nine interconnected perspectives in the fusion matrix. These nine interrelated elements can complement each other to remove the potential bias. In contrast, other fusion methods only employ traditional fusion methods from a limited viewpoint, which can cause insufficient information for different

TABLE V
WE COMPARE IF WITH CNN-PPF, TWO-BRANCH CNN, CONTEXT CNN, ENDNET, MDL-RS, S2FL, CO-CNN, SPECTRALFORMER, MFT, AND IP-CNN ON THE HOUSTON DATASET.

No.	Class	Performance											
		CNN-PPF[18]	Two-branch CNN[11]	Two-branch CNN (Merge)	Context CNN[19]	EndNet[12]	MDL-RS[6]	S2FL[38]	Co-CNN [20]	Spectral former[30]	MFT[39]	IP-CNN[13]	IF
1	Health grass	83.57	83.10	83.10	84.89	81.58	83.10	81.67	98.51	82.65	82.34	85.77	96.58
2	Stressed grass	98.21	84.10	81.20	87.40	83.65	81.58	82.99	97.83	83.33	88.78	87.34	99.44
3	Synthetic grass	98.42	100.00	100.00	99.86	100.00	100.00	100.00	70.60	75.78	98.15	100.00	91.49
4	Tress	97.73	93.09	92.90	93.49	93.09	99.72	92.05	99.06	91.10	94.35	94.26	95.64
5	Soil	96.50	100.00	99.81	99.72	99.91	99.81	99.43	100.00	98.30	99.12	98.42	99.72
6	Water	97.20	99.30	100.00	98.77	95.10	95.10	99.30	41.11	89.04	99.30	99.91	92.31
7	Residential	85.82	92.82	92.54	82.81	82.65	90.02	76.31	83.14	81.72	88.56	94.59	98.23
8	Commercial	56.51	82.34	94.87	78.78	81.29	87.94	68.09	98.39	67.81	86.89	91.81	99.43
9	Road	71.20	84.70	83.85	82.51	88.29	81.59	69.22	94.81	74.47	87.91	89.35	95.18
10	Highway	57.12	65.44	69.89	59.41	89.00	86.68	52.12	92.98	56.76	64.70	72.43	98.65
11	Railway	80.55	88.24	86.15	83.24	83.78	89.37	90.42	90.88	59.93	98.64	96.57	99.62
12	Parking lot 1	62.82	89.53	92.60	92.13	90.39	85.69	87.42	91.02	70.00	94.24	95.60	99.23
13	Parking lot 2	63.86	92.28	79.30	94.88	82.46	83.16	70.18	97.09	66.20	90.29	94.37	94.39
14	Tennis court	100.00	96.76	100.00	99.77	100.00	100.00	100.00	100.00	92.04	99.73	99.86	99.60
15	Running track	98.10	99.79	100.00	98.79	98.10	98.73	98.31	97.85	77.45	99.58	99.99	91.33
	OA (%)	83.33	87.98	88.91	86.90	88.52	89.60	81.95	90.43	76.87	89.80	92.06	97.50
	AA (%)	83.21	90.11	90.42	89.11	89.95	90.83	84.50	90.22	77.77	91.51	93.35	96.72
	Kappa (%)	81.88	86.98	87.96	85.89	87.59	88.75	80.40	89.68	75.03	88.93	91.42	97.29

TABLE VI
WE COMPARE IF WITH CNN-PPF, TWO-BRANCH CNN, CONTEXT CNN, ENDNET, MDL-RS, S2FL, CO-CNN, SPECTRALFORMER, MFT, AND IP-CNN ON THE MUUFL DATASET.

No.	Class	Performance											
		CNN-PPF[18]	Two-branch CNN[11]	Two-branch CNN (Merge)	Context CNN[19]	EndNet [12]	MDL-RS[6]	S2FL [38]	Co-CNN[20]	Spectral former[30]	MFT[39]	IP-CNN[13]	IF
1	Trees	89.07	92.35	94.28	91.29	89.00	88.57	72.40	98.90	97.30	97.90	94.40	98.87
2	Mostly grass	85.71	59.30	82.84	63.09	84.73	84.00	75.97	78.60	69.35	92.11	92.26	96.12
3	Mixed ground surface	80.15	94.47	84.58	81.84	73.39	73.79	54.72	90.66	78.48	91.80	87.96	95.94
4	Dirt and sand	93.10	93.74	97.32	93.92	91.95	93.48	82.20	90.60	82.63	91.59	97.15	99.16
5	Road	88.98	92.76	92.96	89.44	87.72	88.54	71.26	96.90	87.91	95.60	94.38	97.87
6	Water	98.93	98.42	99.05	92.92	99.14	98.42	94.42	75.98	58.77	88.19	99.79	98.42
7	Building shadow	89.07	95.68	93.28	84.73	91.58	90.46	77.34	73.54	85.87	90.27	96.30	97.17
8	Building	92.15	94.01	95.42	81.22	91.30	92.95	86.19	96.66	95.60	97.26	96.13	98.87
9	Sidewalk	75.45	86.64	84.13	81.30	83.75	81.37	59.21	64.93	53.52	61.35	94.01	93.36
10	Yellow curb	100.00	100.00	100.00	98.91	100.00	100.00	98.91	19.47	08.43	17.43	100.00	96.97
11	Cloth panels	100.00	96.64	97.48	99.63	99.63	99.26	98.88	62.76	35.29	72.79	99.63	99.16
	OA (%)	90.97	90.35	91.95	86.07	87.02	87.54	72.49	90.93	88.25	94.34	93.86	97.96
	AA (%)	90.24	91.27	92.58	87.12	90.20	90.14	79.23	77.18	68.47	81.48	95.64	97.45
	Kappa (%)	84.46	87.27	89.35	81.89	83.24	83.31	65.81	88.22	84.40	92.51	91.99	97.27

modalities and contain discrimination from limited views. Therefore, IF can create a novel insight for HSI multi-modal data fusion.

D. Experiments with fusion strategies and patch sizes

In addition, we explore the impact of the change in patch sizes and fusion strategies on the final performance. We compare the performance of four distinct size settings of input data sources, including 3×3 , 6×6 , 9×9 , and 12×12 , with three different fusion strategies settings, including early, middle, and late. In stage 1, we set the number of patches for the input as nine in all situations, which means the small patch size for 3×3 is on the pixel level, while 6×6 , 9×9 and 12×12 are on patch level. As shown in Tables VIII, IX, and X, the 3×3 achieved the worst performance among different fusion strategies in three datasets since pixel-level input has insufficient neighborhood information to explore the relationship between the center patch and nearby patches for

intra- and inter-modalities. When patch size increases, there is a clear increasing tendency, which means the patch size positively affects final performance. It is worth noting that the IF framework can achieve similar performance regardless of distinct fusion strategies when input is on the patch level, which means the IF framework can achieve robust performance on different fusion strategies.

E. Ablation studies

To further study each proposed module’s influence, we conduct ablation studies on the three widely used datasets. To explore the effectiveness of using multi-modality, we implement a model merely based on HSI. With the sufficient information provided by other modality, we can observe a significant improvement of 7.19%, 3.86%, and 3.01% in OA on Houston, Trento, and MUUFL, respectively. It demonstrates that the abundant information in different modalities is crucial to HSI classification. As shown in Fig.5, the element in the

TABLE VII

WE COMPARE IF WITH CNN-PPF, TWO-BRANCH CNN, CONTEXT CNN, ENDNET, MDL-RS, S2FL, CO-CNN, SPECTRALFORMER, MFT, AND IP-CNN ON TRENTO DATASET. MORE SPECIFICALLY, IP-CNN NEEDS TWO-STAGE TRAINING INCLUDING UNSUPERVISED AND SUPERVISED TRAINING WHICH WILL CAUSE INFORMATION LEAKAGE.

No.	Class	Performance											
		CNN-PPF[18]	Two-branch CNN[11]	Two-branch CNN (Merge)	Context CNN[19]	EndNet [12]	MDL-RS[6]	S2FL [38]	Co-CNN[20]	Spectral former[30]	MFT[39]	IP-CNN[13]	IF
1	Apple trees	90.11	98.07	98.51	99.26	88.19	88.58	79.26	99.87	96.76	98.23	99.00	99.15
2	Buildings	83.34	95.21	92.49	86.81	98.49	95.86	92.44	83.84	97.25	99.34	99.40	98.92
3	Ground	71.13	93.32	100.00	97.91	95.19	93.58	92.78	87.09	58.47	89.84	99.10	84.49
4	Woods	99.04	99.93	97.32	97.31	99.30	99.22	94.94	99.98	99.24	99.82	99.92	100.00
5	Vineyard	99.37	98.78	100.00	99.82	91.96	83.82	72.83	99.61	93.52	99.93	99.66	99.94
6	Roads	89.73	89.98	92.56	84.63	90.14	76.51	86.40	98.75	73.39	88.72	90.21	90.14
	OA (%)	94.76	97.92	97.46	96.11	94.17	90.65	83.95	97.69	93.51	98.32	98.58	98.54
	AA (%)	88.97	96.19	96.80	94.29	93.88	89.60	86.44	94.86	86.44	95.98	97.88	95.44
	Kappa (%)	93.04	96.81	96.61	94.81	92.22	86.28	78.99	96.91	91.36	97.75	98.17	98.05

TABLE VIII

THE HOUSTON DATASET PERFORMANCE CHANGE FOLLOWS THE CHANGE OF DIFFERENT FUSION STAGES AND THE SIZE OF INPUT IMAGE

Metric	Early				Middle				Late			
	3 × 3	6 × 6	9 × 9	12 × 12	3 × 3	6 × 6	9 × 9	12 × 12	3 × 3	6 × 6	9 × 9	12 × 12
OA	85.67	94.36	96.37	97.50	84.82	94.02	95.95	96.38	82.74	94.78	93.69	97.03
AA	86.05	93.89	95.42	96.72	84.87	93.25	95.22	95.83	83.11	94.46	93.15	96.52
Kappa	84.46	93.88	96.06	97.29	83.52	93.51	95.60	96.07	81.27	94.33	93.15	96.78

TABLE IX

THE TRENTO DATASET PERFORMANCE CHANGE FOLLOWS THE CHANGE OF DIFFERENT FUSION STAGES AND THE SIZE OF INPUT IMAGE

Metric	Early				Middle				Late			
	3 × 3	6 × 6	9 × 9	12 × 12	3 × 3	6 × 6	9 × 9	12 × 12	3 × 3	6 × 6	9 × 9	12 × 12
OA	97.28	98.24	98.54	98.39	97.05	97.51	98.50	98.33	97.20	97.81	98.37	98.32
AA	93.50	96.18	95.44	96.41	93.18	92.91	95.97	96.00	93.00	93.82	96.04	95.45
Kappa	96.35	97.65	98.05	97.85	96.04	96.66	97.99	97.76	96.24	97.07	97.81	97.75

TABLE X

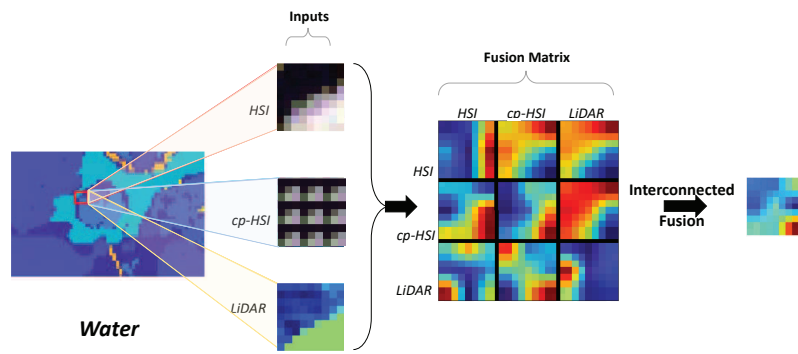
THE MUFL DATASET PERFORMANCE CHANGE FOLLOWS THE CHANGE OF DIFFERENT FUSION STAGES AND THE SIZE OF INPUT IMAGE

Metric	Early				Middle				Late			
	3 × 3	6 × 6	9 × 9	12 × 12	3 × 3	6 × 6	9 × 9	12 × 12	3 × 3	6 × 6	9 × 9	12 × 12
OA	95.49	97.08	97.48	97.84	95.89	97.29	97.73	97.96	95.74	97.09	97.48	97.78
AA	95.56	96.55	97.14	97.54	95.42	96.79	97.51	97.45	95.05	97.04	97.14	97.51
Kappa	94.00	96.11	96.63	97.11	94.50	96.38	96.97	97.27	94.31	96.11	96.63	97.04

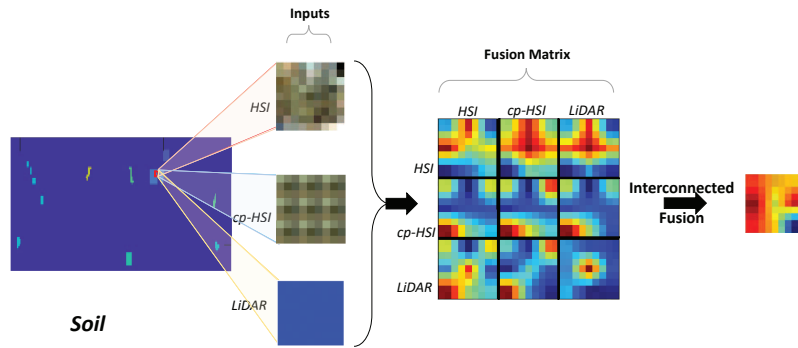
TABLE XI

THE CLASSIFICATION PERFORMANCE OF DIFFERENT ABLATION SETTINGS IS CONDUCTED HERE. WITHOUT THE CONTEXTUAL INFORMATION MEANS REMOVING THE CENTER-PATCH INTRA-MODALITY FEATURE ENCODING MODULE IN STAGE 1. WITHOUT FUSION MATRIX INDICATES COMBINING THE NINE ELEMENTS IN THE FUSION MATRIX THROUGH CONCATENATION. IN ADDITION, HSI MODALITY REPRESENTS IMPLEMENTING A MODEL MERELY BASED ON HSI.

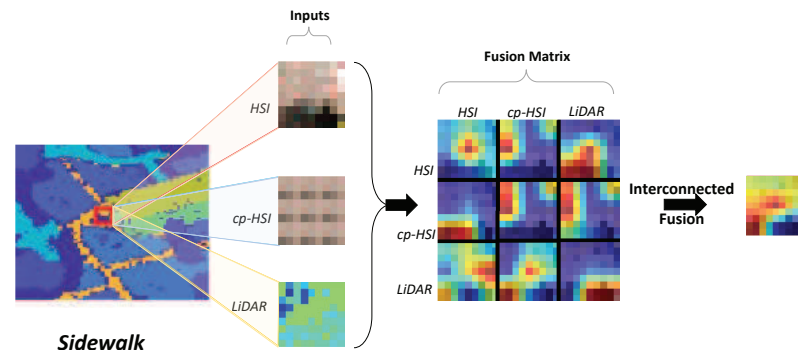
	Metric	Without contextual information	Without fusion matrix	HSI modality	IF framework
Houston	OA	96.41	91.35	90.31	97.50
	AA	95.76	95.31	90.10	96.72
	Kappa	96.10	95.56	88.96	97.29
Trento	OA	97.73	97.51	95.56	98.54
	AA	93.92	95.26	90.97	95.44
	Kappa	96.96	96.67	94.05	98.05
MUUFL	OA	96.47	96.00	95.10	97.96
	AA	96.89	95.82	92.41	97.45
	Kappa	96.25	95.31	93.44	97.27



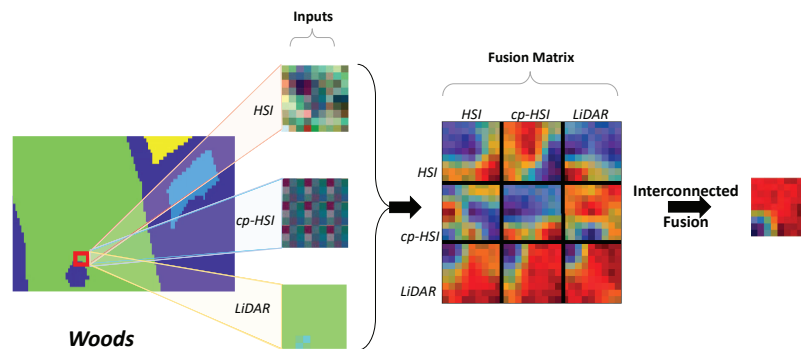
(a) Water



(b) Soil



(c) Sidewalk



(d) Wood

Fig. 5. The three inputs, fusion matrix, and integrated feature after the Interconnected Fusion stage have been visualized. The first input shows the false color visualization of the HSI input. The second input is the center patch of HSI. The third input represents the corresponding LiDAR visualization (blue represents no altitude information). Then the nine perspectives in the fusion matrix have been calculated and visualized. After the Interconnected Fusion Stage, the nine interconnected elements can complement each other and eliminate bias from each perspective.

top-left corner of the fusion matrix refers to the HSI feature. We observe that only utilizing the information of one modality faces challenges in focusing on the correct part of inputs.

Nevertheless, directly fusing the information of different modalities cannot promise a significant improvement in HSI multi-modal classification. To study the influence of the proposed fusion matrix, we combine the nine elements in the fusion matrix through concatenation, replacing the fusion matrix and the feature fusion layer. Compared to the single modality, the multi-modality model using the concatenation layer only improved the metric by 1.04%, 2.05%, and 1.10%, respectively, in OA on Houston, Trento, and MUUFL, which is much less significant than the improvement brought by the proposed fusion matrix. The main reason is that multi-modality also introduces more noise into the model, although it contains more information. However, the proposed fusion matrix can eliminate the negative influence by adaptively adjusting the weights of different modalities. As shown in Fig. 5, the attention of each element in the fusion matrix mainly focuses on the wrong spatial position. However, after the Interconnected fusion stage, the overall attention focuses on proper spatial position, consistent with human perception.

Finally, we remove the center patch intra-modality feature encoding module to implement a model without considering neighborhood relations. We can observe a performance degradation on the model without neighborhood relations by 1.10%, 0.79%, and 1.49%, respectively, in OA on Houston, Trento, and MUUFL. The fact illustrates that the contextual information of the neighborhood patches should also be included in HSI multi-modal classification. As shown in Fig.5, the four vertices of the fusion matrix refer to the fusion matrix without contextual information. The features of these four vertices have the probability of focusing on the wrong part.

V. CONCLUSIONS

We proposed an Interconnected Fusion framework that considers the wealth correlations from different modalities. The contextual information between the center patch and nearby patches can be extracted to enrich the information from intra- and inter-modality. across HSI and LiDAR signals contain intra- and inter-modalities information. In addition, the correlation of intra- and inter-modalities are generated through nine different perspectives in the fusion matrix. These nine interrelated elements in the fusion matrix can complement each other and work together to eliminate bias from each view. Thus, our method can gain an in-depth understanding of the feature fusion for HSI-LiDAR signals.

ACKNOWLEDGMENT

The authors would like to thank the University of Houston and the GRSS-DFC for providing the University of Houston data sets.

REFERENCES

- [1] B. Du, M. Zhang, L. Zhang, R. Hu, and D. Tao, "Pltd: Patch-based low-rank tensor decomposition for hyperspectral images," *IEEE Transactions on Multimedia*, vol. 19, no. 1, pp. 67–79, 2017.
- [2] C. Shi and C.-M. Pun, "Multiscale superpixel-based hyperspectral image classification using recurrent neural networks with stacked autoencoders," *IEEE Transactions on Multimedia*, vol. 22, no. 2, pp. 487–501, 2019.
- [3] P. Bajcsy and P. Groves, "Methodology for hyperspectral band selection," *Photogrammetric Engineering & Remote Sensing*, vol. 70, no. 7, pp. 793–802, 2004.
- [4] D. Landgrebe, "Hyperspectral image data analysis," *IEEE Signal Processing Magazine*, vol. 19, no. 1, pp. 17–28, 2002.
- [5] W. Sun and Q. Du, "Hyperspectral band selection: A review," *IEEE Geoscience and Remote Sensing Magazine*, vol. 7, no. 2, pp. 118–139, 2019.
- [6] D. Hong, L. Gao, N. Yokoya, J. Yao, J. Chanussot, Q. Du, and B. Zhang, "More diverse means better: Multimodal deep learning meets remote-sensing imagery classification," *IEEE Transactions on Geoscience and Remote Sensing*, vol. 59, no. 5, pp. 4340–4354, 2020.
- [7] J. Li, D. Hong, L. Gao, J. Yao, K. Zheng, B. Zhang, and J. Chanussot, "Deep learning in multimodal remote sensing data fusion: A comprehensive review," *arXiv preprint arXiv:2205.01380*, 2022.
- [8] Y.-L. Chang, C.-C. Han, H. Ren, C.-T. Chen, K.-S. Chen, and K.-C. Fan, "Data fusion of hyperspectral and sar images," *Optical Engineering*, vol. 43, no. 8, pp. 1787–1797, 2004.
- [9] B. Huang, Y. Li, X. Han, Y. Cui, W. Li, and R. Li, "Cloud removal from optical satellite imagery with sar imagery using sparse representation," *IEEE Geoscience and Remote Sensing Letters*, vol. 12, no. 5, pp. 1046–1050, 2015.
- [10] C. Debes, A. Merentitis, R. Heremans, J. Hahn, N. Frangiadakis, T. van Kasteren, W. Liao, R. Bellens, A. Pižurica, S. Gautama, W. Philips, S. Prasad, Q. Du, and F. Pacifici, "Hyperspectral and lidar data fusion: Outcome of the 2013 grss data fusion contest," *IEEE Journal of Selected Topics in Applied Earth Observations and Remote Sensing*, vol. 7, no. 6, pp. 2405–2418, 2014.
- [11] X. Xu, W. Li, Q. Ran, Q. Du, L. Gao, and B. Zhang, "Multisource remote sensing data classification based on convolutional neural network," *IEEE Transactions on Geoscience and Remote Sensing*, vol. 56, no. 2, pp. 937–949, 2017.
- [12] D. Hong, L. Gao, R. Hang, B. Zhang, and J. Chanussot, "Deep encoder-decoder networks for classification of hyperspectral and lidar data," *IEEE Geoscience and Remote Sensing Letters*, 2020.
- [13] M. Zhang, W. Li, R. Tao, H. Li, and Q. Du, "Information fusion for classification of hyperspectral and lidar data using ip-cnn," *IEEE Transactions on Geoscience and Remote Sensing*, vol. 60, pp. 1–12, 2021.
- [14] X. Wu, D. Hong, and J. Chanussot, "Convolutional neural networks for multimodal remote sensing data classification," *IEEE Transactions on Geoscience and Remote Sensing*, vol. 60, pp. 1–10, 2021.
- [15] X. Wang, Y. Feng, R. Song, Z. Mu, and C. Song, "Multi-attentive hierarchical dense fusion net for fusion classification of hyperspectral and lidar data," *Information Fusion*, vol. 82, pp. 1–18, 2022.
- [16] P. Xu, X. Zhu, and D. A. Clifton, "Multimodal learning with transformers: a survey," *arXiv preprint arXiv:2206.06488*, 2022.
- [17] W. Wang, D. Tran, and M. Feiszli, "What makes training multimodal classification networks hard?" in *Proceedings of the IEEE/CVF Conference on Computer Vision and Pattern Recognition*, 2020, pp. 12 695–12 705.
- [18] W. Li, G. Wu, F. Zhang, and Q. Du, "Hyperspectral image classification using deep pixel-pair features," *IEEE Transactions on Geoscience and Remote Sensing*, vol. 55, no. 2, pp. 844–853, 2016.
- [19] H. Lee and H. Kwon, "Going deeper with contextual cnn for hyperspectral image classification," *IEEE Transactions on Image Processing*, vol. 26, no. 10, pp. 4843–4855, 2017.
- [20] R. Hang, Z. Li, P. Ghamisi, D. Hong, G. Xia, and Q. Liu, "Classification of hyperspectral and lidar data using coupled cnns," *IEEE Transactions on Geoscience and Remote Sensing*, vol. 58, no. 7, pp. 4939–4950, 2020.
- [21] Y. Chen, H. Jiang, C. Li, X. Jia, and P. Ghamisi, "Deep feature extraction and classification of hyperspectral images based on convolutional neural networks," *IEEE Transactions on Geoscience and Remote Sensing*, vol. 54, no. 10, pp. 6232–6251, 2016.
- [22] L. He, J. Li, C. Liu, and S. Li, "Recent advances on spectral-spatial hyperspectral image classification: An overview and new guidelines," *IEEE Transactions on Geoscience and Remote Sensing*, vol. 56, no. 3, pp. 1579–1597, 2017.
- [23] P. Ghamisi, E. Maggiori, S. Li, R. Souza, Y. Tarabla, G. Moser, A. De Giorgi, L. Fang, Y. Chen, M. Chi, *et al.*, "New frontiers in spectral-spatial hyperspectral image classification: The latest advances based on mathematical morphology, markov random fields, segmenta-

- tion, sparse representation, and deep learning,” *IEEE geoscience and remote sensing magazine*, vol. 6, no. 3, pp. 10–43, 2018.
- [24] Z. Zhong, J. Li, Z. Luo, and M. Chapman, “Spectral–spatial residual network for hyperspectral image classification: A 3-d deep learning framework,” *IEEE Transactions on Geoscience and Remote Sensing*, vol. 56, no. 2, pp. 847–858, 2017.
- [25] S. Jia, J. Liao, M. Xu, Y. Li, J. Zhu, W. Sun, X. Jia, and Q. Li, “3-d gabor convolutional neural network for hyperspectral image classification,” *IEEE Transactions on Geoscience and Remote Sensing*, vol. 60, pp. 1–16, 2022.
- [26] S. K. Roy, D. Hong, P. Kar, X. Wu, X. Liu, and D. Zhao, “Lightweight heterogeneous kernel convolution for hyperspectral image classification with noisy labels,” *IEEE Geoscience and Remote Sensing Letters*, vol. 19, pp. 1–5, 2022.
- [27] A. Plaza, J. A. Benediktsson, J. W. Boardman, J. Brazile, L. Bruzzone, G. Camps-Valls, J. Chanussot, M. Fauvel, P. Gamba, A. Gualtieri, *et al.*, “Recent advances in techniques for hyperspectral image processing,” *Remote sensing of environment*, vol. 113, pp. S110–S122, 2009.
- [28] M. J. Khan, H. S. Khan, A. Yousaf, K. Khurshid, and A. Abbas, “Modern trends in hyperspectral image analysis: A review,” *IEEE Access*, vol. 6, pp. 14 118–14 129, 2018.
- [29] R. Ji, Y. Gao, R. Hong, Q. Liu, D. Tao, and X. Li, “Spectral–spatial constraint hyperspectral image classification,” *IEEE Transactions on Geoscience and Remote Sensing*, vol. 52, no. 3, pp. 1811–1824, 2013.
- [30] D. Hong, Z. Han, J. Yao, L. Gao, B. Zhang, A. Plaza, and J. Chanussot, “Spectralformer: Rethinking hyperspectral image classification with transformers,” *IEEE Transactions on Geoscience and Remote Sensing*, vol. 60, pp. 1–15, 2021.
- [31] S. Amir, Y. Gandelsman, S. Bagon, and T. Dekel, “Deep vit features as dense visual descriptors,” *arXiv preprint arXiv:2112.05814*, vol. 2, no. 3, p. 4, 2021.
- [32] A. Dosovitskiy, L. Beyer, A. Kolesnikov, D. Weissenborn, X. Zhai, T. Unterthiner, M. Dehghani, M. Minderer, G. Heigold, S. Gelly, *et al.*, “An image is worth 16x16 words: Transformers for image recognition at scale,” *arXiv preprint arXiv:2010.11929*, 2020.
- [33] M. M. Naseer, K. Ranasinghe, S. H. Khan, M. Hayat, F. Shahbaz Khan, and M.-H. Yang, “Intriguing properties of vision transformers,” *Advances in Neural Information Processing Systems*, vol. 34, pp. 23 296–23 308, 2021.
- [34] H.-Y. Zhou, C. Lu, S. Yang, and Y. Yu, “Convnets vs. transformers: Whose visual representations are more transferable?” in *Proceedings of the IEEE/CVF International Conference on Computer Vision*, 2021, pp. 2230–2238.
- [35] Z. Zhong, Y. Li, L. Ma, J. Li, and W.-S. Zheng, “Spectral–spatial transformer network for hyperspectral image classification: A factorized architecture search framework,” *IEEE Transactions on Geoscience and Remote Sensing*, vol. 60, pp. 1–15, 2021.
- [36] L. Sun, G. Zhao, Y. Zheng, and Z. Wu, “Spectral–spatial feature tokenization transformer for hyperspectral image classification,” *IEEE Transactions on Geoscience and Remote Sensing*, vol. 60, pp. 1–14, 2022.
- [37] K. Han, Y. Wang, H. Chen, X. Chen, J. Guo, Z. Liu, Y. Tang, A. Xiao, C. Xu, Y. Xu, *et al.*, “A survey on vision transformer,” *IEEE transactions on pattern analysis and machine intelligence*, 2022.
- [38] D. Hong, J. Hu, J. Yao, J. Chanussot, and X. X. Zhu, “Multimodal remote sensing benchmark datasets for land cover classification with a shared and specific feature learning model,” *ISPRS Journal of Photogrammetry and Remote Sensing*, vol. 178, pp. 68–80, 2021.
- [39] S. K. Roy, A. Deria, D. Hong, B. Rasti, A. Plaza, and J. Chanussot, “Multimodal fusion transformer for remote sensing image classification,” *arXiv preprint arXiv:2203.16952*, 2022.
- [40] P. Gader, A. Zare, R. Close, J. Aitken, and G. Tuell, “Mufl gulfport hyperspectral and lidar airborne data set,” *Univ. Florida, Gainesville, FL, USA, Tech. Rep. REP-2013-570*, 2013.
- [41] Z. Liu, H. Mao, C.-Y. Wu, C. Feichtenhofer, T. Darrell, and S. Xie, “A convnet for the 2020s,” in *Proceedings of the IEEE/CVF Conference on Computer Vision and Pattern Recognition*, 2022, pp. 11 976–11 986.

This figure "fig1.png" is available in "png" format from:

<http://arxiv.org/ps/2304.00495v1>